# Defeating Loss Mechanisms in 1D $TiO_2$-Based Hybrid Solar Cells

*A. Wisnet, K. Bader, S. B. Betzler, M. Handloser, P. Ehrenreich, T. Pfadler, J. Weickert, A. Hartschuh, L. Schmidt-Mende, C. Scheu, and J. A. Dorman**

**Titanium dioxide ($TiO_2$) semiconductors are widely used in energy conversion, energy storage, catalysis, and other electronic applications. Hydrothermally grown $TiO_2$ nanowires are an alternative to mesoporous $TiO_2$ nanostructures due to possible direct charge transport, but their full potential waits to be unleashed. Latest findings show a peculiar defect structure, consisting of small single-crystalline fingers and free internal surfaces, which supposedly promote a number of loss mechanisms. In this paper, the influence of these defects on charge transport is studied on the basis of hybrid solar cells featuring a $TiO_2$/dye/polymer interface. Electrical, optical, and structural characterization identifies a number of loss mechanisms, which are inhibited by the introduction of particular annealing steps at specific processing points during fabrication. An increase in power-conversion efficiency of 35% is obtained, resulting in 2.71% and surpassing mesoporous films of the same material combination. These results suggest that caution has to be exercised when dealing with defect structures possibly present in metal oxides which appear single-crystalline by conventional analysis methods.**

## 1. Introduction

Owing to their chemical stability, availability, and intrinsic semiconducting properties, titanium dioxide ($TiO_2$) nanostructures have extensively been studied for application in next-generation technologies such as solar cells, Li-ion battery electrodes, photocatalysts, and memristors.[1] Commonly, 25 nm particle $TiO_2$ films are annealed, forming a high-surface area mesoporous scaffolding, ideal for applications in hybrid, dye-sensitized (DSSC), and perovskite solar cells with devices reaching conversion efficiencies of 3.2%, 12.3%, and 19.3%, respectively.[2] Previously, in an attempt to improve the metal-oxide material, groups have substituted the mesoporous film with nanostructured ones. Here, the $TiO_2$ exists for example as 3D single crystal by using a template method,[3] or as 1D wires when using a hydrothermal method for a natural bottom-up approach.[4–6] While both of these approaches have successfully been implemented into perovskite and solid state (ss)-DSSCs, the improvement was not as drastic as expected. For example, an efficiency improvement of 10% was achieved for the electrochemical ss-DSSC gyroid structure (from 2.67% to 2.97%).[3,7] Alternatively, a semiordered array of rutile nanowires is formed via a hydrothermal growth process directly on a fluorine-doped tin oxide (FTO) substrate. This process allows the separate tuning of wire diameters between 70 and 200 nm and wire lengths up to 10 µm. These nanowires are said to be single-crystalline rutile due to the growth processing, producing a high-mobility electron transporter, roughly 1 $cm^2\ V^{-1}\ s^{-1}$, without the obstacle of multiple grain boundaries during charge transport which is present in the mesoporous films.[8] Additionally, the nanostructured arrays allow for direct transport to the electrode, as opposed to mesoporous diffusive transport. While the hydrothermal nanowires start to grow in a single-crystalline manner, distinct defects and internal surfaces have been reported to appear axially throughout the length of the crystal in what has been called a finger-like structure.[6] The fingers are believed to form due to Coulombic and steric hindrance at the (001) surface present during growth, prohibiting the titanium precursor from reacting and condensing in a uniform single crystal. The structure can be termed a quasi-single crystal, since the fingers merge together in a defect-free structure near the nucleation point. One measure which has been previously discussed, albeit for an alternate reason, is a high-temperature (HT) post-annealing at 500 °C.[9] It was initially concluded that the annealing increased the contact with the FTO substrate while passivating the surface recombination sites at the interface. These effects can also be achieved using an additional $TiCl_4$ treatment and subsequent annealing at 450 °C, which is commonly used for mesoporous films with the additional benefit of increased dye absorption.[10] It is

A. Wisnet, K. Bader, S. B. Betzler, Dr. M. Handloser, Prof. A. Hartschuh, Prof. C. Scheu
Department of Chemistry and
Center for NanoScience (CeNS)
Ludwig Maximilians University
Butenandtstr. 11, 81377 Munich, Germany
P. Ehrenreich, T. Pfadler, Dr. J. Weickert, Prof. L. Schmidt-Mende, Dr. J. A. Dorman
Department of Physics
Konstanz University
Universitätstr. 10, 78457 Konstanz, Germany
E-mail: James.Dorman@uni-konstanz.de
Prof. C. Scheu
Max-Planck-Institut für Eisenforschung GmbH
40237 Düsseldorf, Germany

**DOI: 10.1002/adfm.201404010**

necessary to understand the role of defects in general, and the finger-like structures in particular, with regard to loss mechanisms and electrical performance in $TiO_2$ devices, where electron transport is vital. Photovoltaic devices are a suitable model system to extract the photophysical and electronic properties of such $TiO_2$ electrodes.

In this work, the relationship of annealing and chemical treatment, crystal defect structure and charge transport in the nanowires is probed in order to develop strategies to enhance the electrical conductivity of the electrode. With this approach the band structure and defect density near the metal oxide-polymer interface is engineered, allowing for direct control of the charge density and mobility. HT annealing makes it possible to eliminate the fingers, simultaneously reducing recombination sites, and thus canceling a number of loss mechanisms. A combination of electrical, optical, and structural characterization techniques is used to investigate the role of the finger structures and crystal defects in general, and a model is developed to describe the carrier transport in hybrid and DSSC-type solar devices. Scanning- (SEM) and transmission electron microscopy (TEM) give insight into morphology and crystal characteristics. Charge recombination is discussed using time-resolved photoluminescence (PL), transient photovoltage (TPV), and impedance spectroscopy (IS), all of which indicate a reduction of radiative trap state-assisted recombination typical for these structures, favoring nonradiative and/or long-living recombination mechanisms after annealing at elevated temperatures. Additionally, a noticeable improvement is seen when comparing these hybrid nanowire devices to their mesoporous counterparts, as reported in literature, with similar material combination. It is expected that these results can be extended to Li batteries and photocatalysts, where rapid transport of charges through a trap-free energy landscape is necessary for improved device performance. In general, our findings indicate that the crystal quality of metal oxides ought to be carefully examined to counter detrimental effects.

## 2. Results and Discussion

Nanowire arrays with nanowire dimensions of ≈80–100 nm in diameter and 1 µm in length were grown using the hydrothermal method reported previously.[5] A $TiCl_4$ treatment was conducted in order to mitigate surface defects and to increase the total surface area by roughening of the surface layer. After an initially single-crystalline growth, the wires tend to form a finger structure featuring free internal surfaces parallel to the wire during growth due to a combination of steric and Coulombic repulsion at the (001) growth layer, as recently discussed.[6] In order to remove these finger structures, the annealing temperature of some samples was increased from 450 to 600 °C at two distinct times during the sample fabrication process: before (Sample 600/450) and after (Sample 450/600) the $TiCl_4$ treatment. These two annealing points were chosen in order to distinguish the role of annealing on the wire structure from that of the shell structure which requires an annealing step. A reference sample was annealed two times at 450 °C (Sample 450/450). A detailed description of the synthesis procedure can be found in the Supporting Information. High-resolution SEM images of the nanowire arrays are shown in **Figure 1**a–c, highlighting the change in surface structure with annealing processes (low-magnification top views in Figure S1, Supporting Information). A rough, dense layer is observed in the case of Samples 450/450 (a) and 600/450 (b), resulting in a high surface area where dye adsorption and charge separation can occur. When the HT annealing occurs after the $TiCl_4$ treatment for Sample 450/600 (c), the surface roughness appears to decrease with only small bumps located across the wires. Dye loading of each surface confirms a slightly lower surface area as expected, from $1.77 \times 10^{19}$ molecules $cm^{-2}$ of substrate for Samples 450/450 and 600/450 to $1.52 \times 10^{19}$ molecules $cm^{-2}$ for Sample 450/600. These values are roughly 3× lower than the mesoporous film with a dye loading of $5.33 \times 10^{19}$ molecules $cm^{-2}$. For all cases, the annealing does not fully remove the truncated finger structure at the tip of each wire. No distinct difference was seen in X-ray diffraction (XRD) spectra after different annealing temperatures since the nanowires naturally form a rutile crystal structure and the volume of the shell layer is below the sensitivity of the measurement (shell thickness < 2 nm) (Figure S2, Supporting Information). Figure 1d–f shows detailed high-resolution TEM (HRTEM) images of the respective samples (bright-field images of the wires are shown in Figure S3, Supporting Information). The particles attached to the wire surfaces usually have a thickness of about 5 nm. Particles found in Samples 450/450 (d) and 600/450 (e) can be attributed to anatase ({101} anatase lattice planes marked by an asterisk), while Sample 450/600 (f) features rutile particles which are epitaxially bonded to the wire. This coincides with the observations made in Figure 1c and suggests that the $TiCl_4$ treatment forms a polycrystalline anatase layer after annealing at 450 °C, but transforms to rutile during the 600 °C annealing. The atomic arrangement of the wire core acts as a seed layer for the epitaxial rearrangement of the shell layer. Scanning TEM (STEM) images of the three samples are presented in Figure 1g–i. The contrast in Sample 450/450 (g) shows stripes running along the length of the wire, indicating a finger structure in the hydrothermally grown core throughout the length of the wire.[6] Compared to this, Samples 600/450 (h) and 450/600 (i) show homogeneous single-crystalline areas at the edge of the wires, while their cores feature a number of voids. These features are a result of the annealing steps at 600 °C which allows for diffusion processes as discussed on the basis of Figure S4, Supporting Information. The volume previously enclosed by the free internal surfaces (the finger structure) is accumulated as voids roughly resembling the Wulff shape of rutile.

In order to quantify light scattering within the nanowire arrays, wavelength-dependent haze measurements were performed on the arrays at different points in the fabrication process, shown in Figure S5, Supporting Information.[11] Differences in scattering behavior of the samples according to annealing treatment are near the range of the error margins within a given batch and no trend could be found favoring Sample 600/450.

PL spectra of bundles of nanowires from the three different samples were taken after femtosecond-pulsed excitation at 800 nm. The investigated material volume was kept larger than the excitation volume (pump flux was kept constant) for each sample during the measurement to allow for comparing the

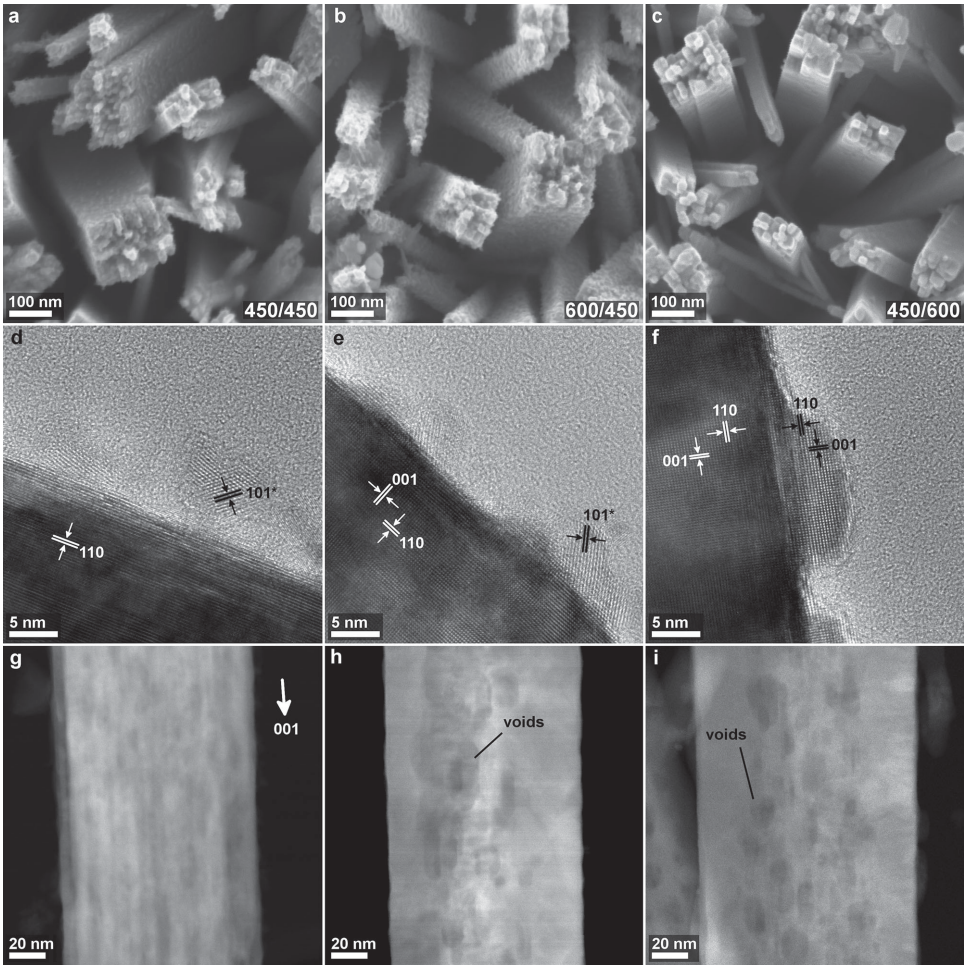


**Figure 1.** High-magnification SEM images of a) Sample 450/450, b) Sample 600/450, and c) Sample 450/600 show the surface roughness and external finger structure after the annealing treatment. d–f) HRTEM images show the rutile modification for the wires. d,e) Particles featuring the anatase crystal structure are found for Samples 450/450 and 600/450 (indices marked by an asterisk). Sample 450/600 shows rutile particles which attached epitaxially during annealing of the wire. g–i) STEM images of the respective wires show that annealing at 450 °C does not considerably change the finger structure, which can be identified by brighter lines along the nanowires in (g). Annealing at 600 °C results in homogeneous single crystalline areas at the outer edges of the wires, while voids are formed inside the wires (h,i).

resulting PL intensities. For $TiO_2$, the PL emission is mainly generated by emissive trap states at the surface of the material, as described before,[12] and is strongly influenced by different fabrication methods or annealing treatments.[12,13] In **Figure 2**a, the PL spectra after two-photon excitation of the different sample types are shown. They are spatially averaged to minimize the influence of heterogeneities. The spectrally broad PL signal is roughly centered around 820 nm reflecting

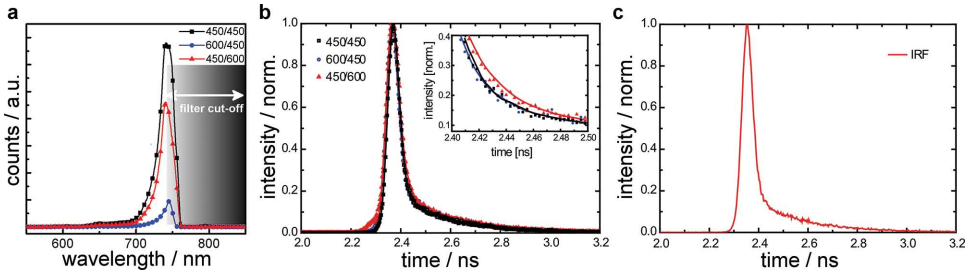


**Figure 2.** a) PL spectra after two-photon excitation at 1.55 eV. The suppressed excitation pulse is indicated by the gray shaded area. Sample 450/450 exhibits the highest signal intensity. Direct quenching of the PL emission after annealing is stronger for Sample 600/450 than for Sample 450/600, indicating a fast nonradiative recombination channel in the former. b) TCSPC characteristics are measured after a short excitation pulse. The inset shows the detailed area of interest. Resulting lifetimes are listed in Table 1. c) Instrument response function for (b). A FWHM of ≈20 ps in combination with the ultrashort excitation pulse of 150 fs allows for a time resolution of 3 ps.[13] Additional experimental details can be found in the Supporting Information.

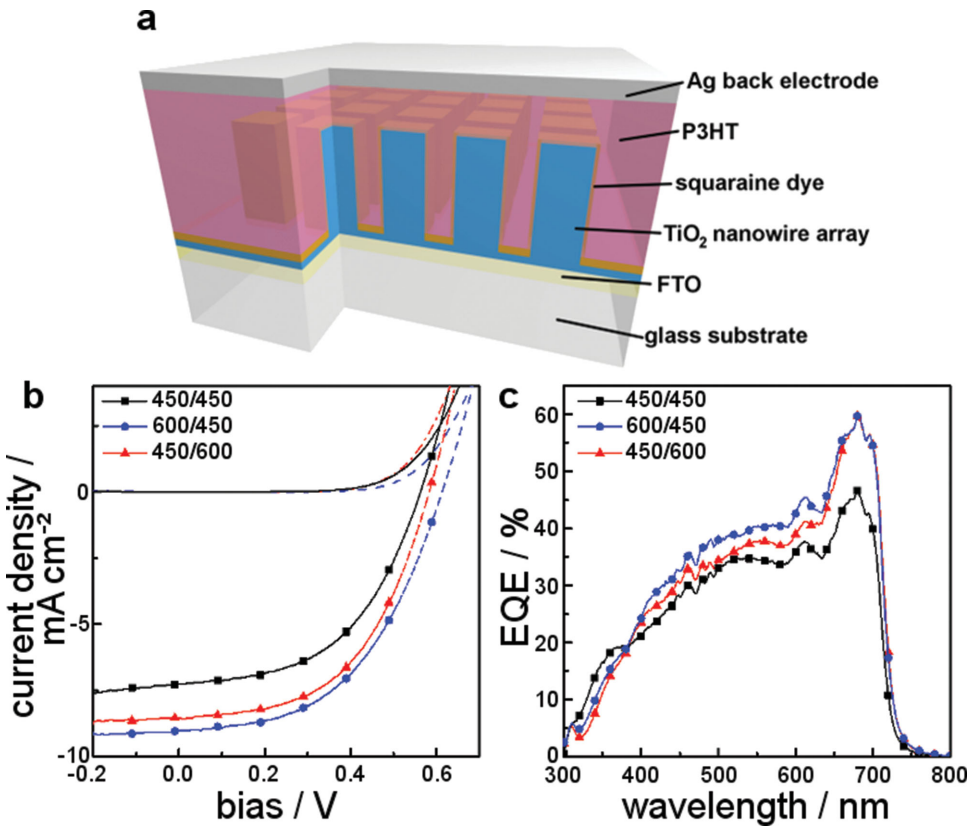


**Figure 3.** a) Schematic of the device structure. b) *J–V* curves for the three samples show increased $J_{SC}$ and $V_{OC}$ for the samples annealed at higher temperatures, with Sample 600/450 providing the highest PCE (see Table 1). c) EQE spectra for the respective samples.

the value reported in literature.[12] Sample 450/450 features the highest PL intensity and thus quantum yield, assuming constant absorption cross sections for all samples. Sample 450/600 still exhibits a considerably stronger signal than Sample 600/450 visible at the signal onset just before the filter cut-off. The intensity data were complemented with PL lifetime measurements using time-correlated single photon counting (TCSPC) with a time resolution of about 3 ps to distinguish radiative and nonradiative decay rates (Figure 2b).[14] This technique is independent of the investigated material volume. For Sample 450/450, an intensity averaged lifetime of about 10 ps was observed pointing toward a fast radiative decay at emissive trap states, which gives a high intensity due to the large number thereof. Sample 600/450 features a similar lifetime of 9 ps, but connected to a much lower PL intensity. This indicates faster nonradiative recombination, suppressing the radiative decay predominant in Sample 450/450, leading to a lower quantum yield and thus weaker PL. The faster nonradiative decay could result from a reduced trap density and the anatase shell layer introducing a band bending that facilitates charge separation, preventing radiative recombination but opening a nonradiative channel at the interface.[15] Sample 450/600 features neither an internal defect structure, nor the external anatase–rutile interface. This is prominently demonstrated by a substantially longer PL lifetime of 21 ps. However, the electron–hole pairs can possibly also recombine in the "bulk" of the nanowires at slower rates, displaying an additional radiative recombination channel visible in the increased fraction of the slow component used in the fit-routine to obtain the presented intensity averaged lifetime values. This channel is probably suppressed in Sample 600/450 due to the fast, nonradiative decay. Hence, the interface between anatase shell layer and rutile wire facilitates the charge separation, while the absence of internal surfaces results in a substantial decrease of recombination sites within the charge-transporting wires, underlining the suitability of Sample 600/450 for solar-cell applications.

To demonstrate the influence of the finger structures on the performance of a photovoltaic device, inverted hybrid devices were fabricated using a squaraine dye (SQ2) as a light absorber and poly(3-hexylthiophene) (P3HT) as a hole transport layer (**Figure 3**a). This material combination was specifically chosen due to the alignment of the lowest unoccupied molecular orbital (LUMO) of SQ2 being between that of the P3HT and the conduction band of the $TiO_2$, allowing for charge extraction from both, SQ2 and P3HT.[16] Absorption spectra of SQ2 on the three different $TiO_2$ surfaces show a change in the aggregation of dye molecules depending on annealing treatment, leading to an enhanced absorption of higher energies in Sample 600/450 (Figure S6, Supporting Information). One possible reason for the increase in light absorption for Sample 600/450 is due to an increased density of defect states between the annealed rutile and anatase layer, as discussed by Llansola-Portoles et al.[17] These defect states could expedite the reduced PL lifetimes discussed above. While it is unclear why they are not seen for

**Table 1.** The key figures of merit including short circuit current density ($J_{SC}$), open circuit voltage ($V_{OC}$), fill factor (FF), and conversion efficiency ($\eta$) are collected for the working devices. Additional values are included to highlight recombination, such as the quality factor ($\alpha$), TPV recombination lifetimes ($\tau_{Rec}$), and $TiO_2$ PL emission lifetimes ($\tau$).

| Sample | $J_{SC}$ [mA cm$^{-2}$] | $V_{OC}$ [V] | FF [%] | $\eta$ [%] | $\alpha$ | $\tau_{Rec}$ (TPV) [µs] | $\tau$ (PL) [ps] |
|---|---|---|---|---|---|---|---|
| Mesoporous | –5.50 | 0.642 | 58 | 2.06 | 0.853 | 80 | K |
| 450/450 | –7.27 | 0.564 | 51 | 2.03 | 0.936 | 88 | 10 |
| 600/450 | –9.02 | 0.614 | 50 | 2.71 | 0.980 | 81 | 9 |
| 450/600 | –8.26 | 0.585 | 53 | 2.53 | 0.976 | 106 | 21 |

Sample 450/450, it is believed that Sample 450/600 causes the rearrangement of the $TiCl_4$-induced layer for the removal of these states. *J–V* curves with and without illumination were measured for the three sample types, with the best performance for each device being plotted (Figure 3b). After annealing, the devices show a sound improvement in performance due to increases in both, the short-current density ($J_{SC}$) and open-circuit voltage ($V_{OC}$), as can be seen in **Table 1**. For comparison, a mesoporous $TiO_2$ device is included in Table 1 (characteristics in Figure S7, Supporting Information). The mesoporous device thickness is roughly 500–700 nm and comparable to current literature results for this material combination.[16,18] The experiments were repeated several times with all sample sets showing the same trend, indicating that the improvement is not due to individual deviations. Additional experimental results can be found in the Supporting Information for a second sample set (Figure S8, Supporting Information).[19] Sample 450/450 exhibited a $J_{SC} = -7.27$ mA cm$^{-2}$ and $V_{OC} = 0.57$ V ($\eta = 2.03\%$). In contrast, Sample 600/450 produced a $J_{SC} = -9.02$ mA cm$^{-2}$ and $V_{OC} = 0.61$ V ($\eta = 2.71\%$) compared to that of Sample 450/600 at $J_{SC} = -8.54$ mA cm$^{-2}$ and $V_{OC} = 0.59$ V ($\eta = 2.53\%$). An overall statistical analysis for multiple batches is shown in Table S1, Supporting Information, and indicates that the trend is consistent with device processing. The mesoporous devices resulted in a slightly lower $J_{SC}$ of –5.50 mA cm$^{-2}$ but the overall efficiency was greater than that of Sample 450/450 ($\eta = 2.26\%$) due to the higher $V_{OC}$ and FF.[16,18,20] The increases in these values are likely due to the slightly higher conduction band of the anatase nanoparticles compared to the rutile nanowires. The lower current is attributed to losses at grain boundaries and a decrease in light absorption, likely due to light scattering of the nanowires which is not present in the mesoporous film. A thicker mesoporous layer would account for this issue but results in a decrease in polymer infiltration and increased charge recombination.

Charge generation was investigated by measuring the external quantum efficiency (EQE), shown in Figure 3c. In comparison, Sample 450/450 shows reduced charge generation across the whole spectrum except a small region in the range of 350–380 nm. This feature can be attributed to the defects within the core which are removed during HT annealing in the other two samples, leading to a diminished charge generation within the $TiO_2$. The increase of charge generation within the dye is similarly enhanced for both of these two samples at its main peak at 670 nm, while the second peak related to the dye (at 615 nm) and the whole region related to absorption in P3HT exhibits the highest EQE for Sample 600/450. This suggests that the main SQ2 EQE feature is limited through light absorption after annealing and no longer through charge injection into the $TiO_2$, in contrast to the other regions of the spectrum. Furthermore, this indicates that the difference in light scattering discussed previously is unlikely to be a phenomenon due to processing conditions. Presumably, the increase in the P3HT generated charges is due to the presence of slightly more defect states, as discussed above, to increase charge injection into the metal oxide layer.[17] An additional reason for this decrease in EQE can be linked to the surface area of the nanowires mentioned above. Therefore, it is difficult to pinpoint the exact mechanism at this moment and will be the subject of further studies, such as transient absorption spectroscopy. The different behavior between Samples 600/450 and 450/600 at the peak of 615 nm is likely related to the aggregation of the dye, as discussed on the basis of the absorption peak in Figure S6, Supporting Information.

The charge transport within the devices was probed by intensity-dependent measurements, and lifetimes of the charges were extracted from transient photodecay measurements (full description in Figure S9, Supporting Information). Fitting $J_{SC}$ as a function of light intensity using the relationship $J_{SC} = \beta P^{\alpha}$ ($P$ as incident light power, $\alpha$ and $\beta$ power law coefficients) gives the quality factor $\alpha$, serving as an indicator for trap state recombination.[21] Consequently, the respective values of $\alpha = 0.936$ for Sample 450/450, $\alpha = 0.980$ for Sample 600/450, and $\alpha = 0.976$ for Sample 450/600 correspond to a strongly reduced number of trap states in the latter two samples. Transient photovoltage decay (TPV) curves showed a decreasing carrier lifetime for increasing background illumination intensities. The related charge recombination lifetimes resulted in 88 µs for Sample 450/450, 81 µs for Sample 600/450, and 106 µs for Sample 450/600 at standard illumination, reflecting the trend shown by the PL measurements. It is noticeable that the recombination at short circuit conditions is lowest for the annealed samples but the recombination under open circuit conditions for the PL and TPV is higher for Sample 600/450. Again, the higher open-circuit recombination might be attributed to the increased surface defect states for Sample 600/450 while the short circuit recombination is decreased due to two factors. First, the surface defect states of the anatase shell are partly above the conduction band of the rutile core,[17] and second, the increased crystallinity of the core reduces the concentration of electrons near these trap states and the amount of recombination events that can occur.

Finally, to probe the dynamics under various working conditions, and in particular around the maximum power point, IS

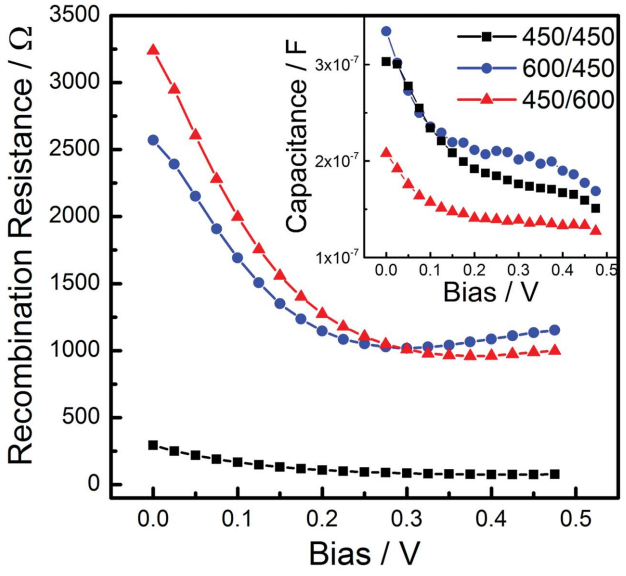


**Figure 4.** Recombination resistance ($R_{Rec}$) and chemical capacitance ($C_\mu$, inset) are plotted as a function of bias voltage from the model IS data. The model used can be found in Figure S8, Supporting Information. An order of magnitude increase in $R_{Rec}$ is seen after annealing the nanowire arrays at 600 °C. The $R_{Rec}$ of the annealed wires have a crossover around 0.3 V. The $C_\mu$ trend observed matches the recombination lifetimes extracted from the TPV data.

measurements were conducted with and without illumination between 0 and 0.5 V bias. The measured impedance curves were simulated using the model shown in Figure S10, Supporting Information. In this model, a series of parallel RC circuits represents the interface between $TiO_2$ and the organic along the nanowire side walls. An additional RC circuit is included in order to allow for successful data modeling, which is attributed to effects due to slightly non-Ohmic external contacts. The results of the fitting for the recombination resistance ($R_{Rec}$) and the chemical potential ($C_\mu$) are plotted in **Figure 4**. The annealing increases $R_{Rec}$ by an order of magnitude across the full bias range, which corroborates with the increased current densities discussed above. At low biases $R_{Rec}$ is lower for the 600/450 sample than that of the 450/600 sample but this trend inverts around 0.3 V, resulting in a slightly higher $R_{Rec}$ at the maximum power point. The probable cause of this inversion is the interfacial area changed by the annealing process. Specifically, at low forward bias, charges are transported through diffusion, increasing the recombination probability at the imperfect $TiO_2$/dye/P3HT interface of Sample 600/450 due to residual recombination sites within the anatase shell layer, as against to the defect-free rutile surface of Sample 450/600, agreeing with the lifetime results mentioned above and the results from Llansola-Portoles et al.[17] At higher forward biases, the charges are not extracted as quickly but the energy offset between the rutile and anatase phases prevents the electrons from reaching the active interface in Sample 600/450, thus reducing the recombination probability. Sample 450/600 does not feature this step in the conduction band, and thus suffers from enhanced recombination at the interface. When $C_\mu$ is plotted as a function of the bias voltage the capacitance decreases when approaching $V_{OC}$ (inset). Furthermore, $C_\mu$ shows an inverse trend to the TPV measurements with Sample 450/450 between the high capacitance of Sample 600/450 and the low one in Sample 450/600, indicating a higher charge density in the 600/450 sample and lowest in the 450/600 sample.[22] This is attributed to the shell layer, which allows a higher amount of separated charges (electrons in $TiO_2$, holes in P3HT) near the interface in case of the anatase shell due to the step in the conduction band for Sample 600/450. The absence of this step allows free spreading of the electrons in Sample 450/600, considerably lowering $C_\mu$.

Based on the electrical, optical, and structural characterizations, a summarizing schematic is presented in **Figure 5** to explain the various loss mechanisms present within the system. Sample 600/450 significantly outperforms both, Sample 450/450 and Sample 450/600, in efficiency (2.71% vs 2.03% and 2.53%) due to a quenching in the charge recombination. This is visible in the reduced charge trap density proven by PL, highest EQE, and highest recombination resistance near the maximum power point. Lowest lifetime in TPV measurements indicate the highest electron mobility. This improvement is underlined by increased $V_{OC}$ and $J_{SC}$. These qualities are rendered possible by: i) a good charge separation made possible via the thin anatase layer covering the rutile core of the wires, introducing a cascading conduction band descending from dye to shell to core, which has been shown to play a beneficial role; ii) removal of free internal surfaces (i.e., the fingers) and the consequential possibility for charges to spread throughout the nanowires; and iii) a strong reduction of charge traps due to a cured and mostly defect-free electrode made up by the rutile wire array. The voids which are observed in TEM apparently do not have a severe detrimental effect. As Sample 450/600 is lacking the anatase layer and thus the band cascade, electrons near the $TiO_2$/dye interface run the risk of recombining with newly created adjacent holes within the dye layer.

## 3. Conclusion

Hydrothermally grown rutile nanowires were subjected to chemical $TiCl_4$ treatment and a series of HT annealing steps. This enabled the elucidation of the relationship between defect structure and charge dynamics when used as an electrode material, with the aim to identify loss mechanisms detrimental to device performance. By annealing the nanowire arrays at different time points within the fabrication process, it was possible to selectively probe both, the role of the finger structures that naturally form during the growth process and the function of the shell layer on charge separation and transport. The higher annealing temperatures generally boosted device performance. The best overall device performance of 2.71% (a 35% improvement compared to the reference) was obtained when the samples were annealed at 600 °C before the $TiCl_4$ surface treatment. In this case, the nanowire core was allowed to rearrange, forming a single crystal throughout the length of the wire, while an anatase shell was formed during the second annealing at 450 °C after the $TiCl_4$ treatment. This process countered three major loss mechanisms within the rutile wires: i) recombination at the active interface, ii) the confinement of electrons within a narrow spatial band promoting enhanced recombination, and iii) a multitude of trap states within the rutile wire

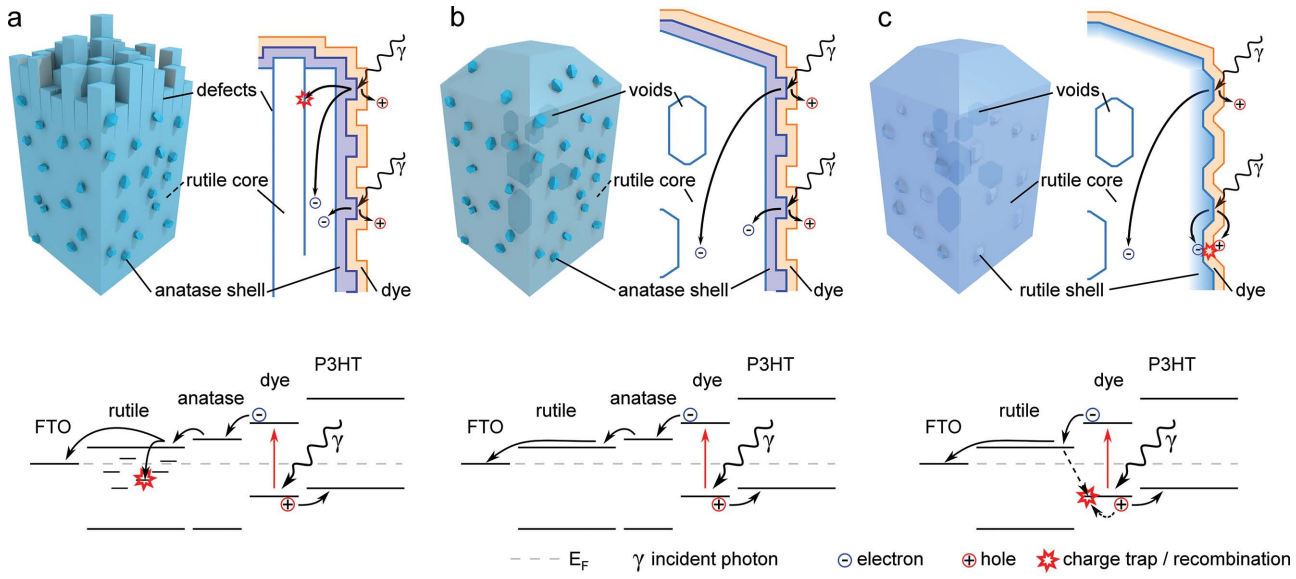


**Figure 5.** A schematic to illustrate the effect of annealing on the nanowire arrays at various time points in the fabrication process: a) 450/450, b) 600/450, c) 450/600. After annealing at higher temperatures, the finger structures that form during the growth process are converted into voids within the wire. Additionally, the shell layer is converted to a rutile film when annealed after $TiCl_4$ treatment in (c). The generated electron is able to move throughout the whole of the nanowire structure in (b,c), instead of an individual finger as in (a). Furthermore, the probability of recombination is decreased with a pre-$TiCl_4$ annealing (a,b) due to the formation of the anatase shell layer which decreases the electron density at the shell. A brief energy level scheme is presented for each sample to highlight the location of trap states and charge recombination possibilities that are present in the device.

core at the free internal surfaces enfolding the fingers. While voids in the wire could be detected after the annealing at 600 °C, they had no observable negative impact on device performance. EQE measurements indicated that the annealing process allowed for more efficient communication with both the dye and polymer, the latter of which was influenced by the crystal type of the shell layer. The devices with the best performance showed an overall decrease in the recombination lifetime, probed using both TPV and PL of the $TiO_2$ wires, which indicated a fast nonradiative recombination channel opened by the anatase shell layer when charges are not extracted. A shell layer of rutile instead of anatase increased the electron lifetimes in all characterization methods, suggesting the need to take an effort to understand and engineer the alignment of the energy levels within devices. However, a more thorough investigation involving transient absorption spectroscopy is required to elucidate the exact recombination mechanisms. In general, the presented results strongly suggest that particular caution has to be exercised when dealing with metal-oxide structures. Crystal defects might not be discerned easily in SEM and XRD data, yet still have major influence on device performance, whether that be photovoltaics, energy storage, or catalysis.

## Supporting Information

Supporting Information is available from the Wiley Online Library or from the author.

## Acknowledgements

We acknowledge the support from the German Research Foundation (DFG) for the projects "SCHE634/10-1: Identification and overcoming of loss mechanisms in nanostructured hybrid solar cells—pathways to more efficient devices," "SPP1355: Elementary processes of organic photovoltaics" and the Nanosystems Initiative Munich. J.A.D. acknowledges the Alexander von Humboldt Foundation post-doctoral research fellowship. J.W. acknowledges support of the Carl Zeiss Foundation through a post-doctoral fellowship. We would also like to thank Matthias Hagner for his support in the Nanostructure Laboratory at the University of Konstanz and Tina Reuther for XRD measurements.

Received: November 12, 2014
Revised: February 7, 2015
Published online: March 18, 2015

[1] a) X. Chen, S. S. Mao, *Chem. Rev.* **2007**, *107*, 2891; b) A. R. Armstrong, G. Armstrong, J. Canales, R. García, P. G. Bruce, *Adv. Mater.* **2005**, *17*, 862; c) J. Wu, R. L. McCreery, *J. Electrochem. Soc.* **2009**, *156*, 29; d) L. Kavan, M. Kalbáč, M. Zukalová, I. Exnar, V. Lorenzen, R. Nesper, M. Graetzel, *Chem. Mater.* **2004**, *16*, 477; e) S. N. Habisreutinger, L. Schmidt-Mende, J. K. Stolarczyk, *Angew. Chem., Int. Ed.* **2013**, *52*, 7372.
[2] a) G. K. Mor, S. Kim, M. Paulose, O. K. Varghese, K. Shankar, J. Basham, C. A. Grimes, *Nano Lett.* **2009**, *9*, 4250; b) A. Yella, H.-W. Lee, H. N. Tsao, C. Yi, A. K. Chandiran, K. Nazeeruddin, E. W.-G. Diau, C.-Y. Yeh, S. M. Zakeeruddin, M. Grätzel, *Science* **2011**, *344*, 629; c) S. A. Breitschneider, J. Weickert, J. A. Dorman, L. Schmidt-Mende, *APL Mater.* **2014**, *2*, 040701; d) H. Zhou, Q. Chen, G. Li, S. Luo, T.-B. Song, H.-S. Duan, Z. Hong, J. You, Y. Liu, Y. Yang, *Science* **2014**, *345*, 542.
[3] E. J. W. Crossland, N. Noel, V. Sivaram, T. Leijtens, J. A. Alexander-Webber, H. J. Snaith, *Nature* **2013**, *495*, 215.
[4] a) J. A. Dorman, J. Weickert, J. B. Reindl, M. Putnik, A. Wisnet, M. Noebels, C. Scheu, L. Schmidt-Mende, *J. Phys. Chem. C* **2014**, *118*, 16672; b) X. Feng, K. Zhu, A. J. Frank, C. A. Grimes, T. E. Mallouk, *Angew. Chem., Int. Ed.* **2012**, *124*, 2781.

[5] B. Liu, E. S. Aydil, *J. Am. Chem. Soc.* **2009**, *131*, 3985.
[6] A. Wisnet, S. B. Betzler, R. V. Zucker, J. A. Dorman, P. Wagatha, S. Matich, E. Okunishi, L. Schmidt-Mende, C. Scheu, *Cryst. Growth Des.* **2014**, *14*, 4658.
[7] E. J. W. Crossland, M. Nedelcu, C. Ducati, S. Ludwigs, M. A. Hillmyer, U. Steiner, H. J. Snaith, *Nano Lett.* **2009**, *9*, 2813.
[8] E. Hendry, M. Koeberg, B. O'Regan, M. Bonn, *Nano Lett.* **2006**, *6*, 755.
[9] Y. Zhao, X. Gu, Y. Qiang, *Thin Solid Films* **2012**, *520*, 2814.
[10] A. Hagfeldt, G. Boschloo, L. Sun, L. Kloo, H. Pettersson, *Chem. Rev.* **2010**, *110*, 6595.
[11] L. Passoni, F. Ghods, P. Docampo, A. Abrusci, J. Martí-Rujas, M. Ghidelli, G. Divitini, C. Ducati, M. Binda, S. Guarnera, A. Li Bassi, C. S. Casari, H. J. Snaith, A. Petrozza, F. Di Fonzo, *ACS Nano* **2013**, *7*, 10023.
[12] X. Wang, Z. Feng, J. Shi, G. Jia, S. Shen, J. Zhou, C. Li, *Phys. Chem. Chem. Phys.* **2010**, *12*, 7083.
[13] a) H. Sezen, M. Buchholz, A. Nefedov, C. Natzeck, S. Heissler, C. Di Valentin, C. Wöll, *Sci. Rep.* **2014**, *4*, 3808; b) T. Berger, T. Lana-Villarreal, D. Monllor-Satoca, R. Gómez, *J. Phys. Chem. C* **2007**, *111*, 9936.
[14] T. Gokus, L. Cognet, J. G. Duque, M. Pasquali, A. Hartschuh, B. Lounis, *J. Phys. Chem. C* **2010**, *114*, 14025.
[15] J.-S. Yang, W.-P. Liao, J.-J. Wu, *ACS Appl. Mater. Interfaces* **2013**, *5*, 7425.
[16] J. Weickert, E. Zimmermann, J. B. Reindl, T. Pfadler, J. A. Dorman, A. Petrozza, L. Schmidt-Mende, *APL Mater.* **2013**, *1*, 042109.
[17] M. J. Llansola-Portoles, J. J. Bergkamp, D. Finkelstein-Shapiro, B. D. Sherman, G. Kodis, N. M. Dimitrijevic, D. Gust, T. A. Moore, A. L. Moore, *J. Phys. Chem. A* **2014**, *118*, 10631.
[18] P. Ehrenreich, T. Pfadler, F. Paquin, L.-I. Dion-Bertrand, O. Paré-Labrosse, C. Silva, J. Weickert, L. Schmidt-Mende, *Phys. Rev. B* **2015**, *91*, 035304.
[19] E. Zimmermann, P. Ehrenreich, T. Pfadler, J. A. Dorman, J. Weickert, L. Schmidt-Mende, *Nat. Photon.* **2014**, *8*, 669.
[20] E. V. Canesi, M. Binda, A. Abate, S. Guarnera, L. Moretti, V. D'Innocenzo, R. S. S. Kumar, C. Bertarelli, A. Abrusci, H. Snaith, A. Calloni, A. Brambilla, F. Ciccacci, S. Aghion, F. Moia, R. Ferragut, C. Melis, G. Malloci, A. Mattoni, G. Lanzani, A. Petrozza, *Energy Environ. Sci.* **2012**, *5*, 9068.
[21] J. van de Lagemaat, N. G. Park, A. J. Frank, *J. Phys. Chem. B* **2000**, *104*, 2044.
[22] J. Bisquert, *Phys. Chem. Chem. Phys.* **2003**, *5*, 5360.